IEEE Access
Multidisciplinary | Rapid Review | Open Access Journal

Received 6 May 2022, accepted 24 June 2022, date of publication 28 June 2022, date of current version 5 July 2022.

Digital Object Identifier 10.1109/ACCESS.2022.3186906

RESEARCH ARTICLE

Photovoltaic Partial Shading Performance Evaluation With a DSTATCOM Controller

BIBHUTI BHUSAN RATH[1], MANOJ KUMAR PANDA[1], (Senior Member, IEEE), BHOLA JHA[1], AROBINDA DASH[2], (Graduate Student Member, IEEE), SURYA PRAKASH[2], (Graduate Student Member, IEEE), RANJAN KUMAR BEHERA[2], (Senior Member, IEEE), KHALIFA AL HOSANI[3], (Senior Member, IEEE), SRINIVASARAO TEGALA[4], (Member, IEEE), AND UTKAL RANJAN MUDULI[3], (Member, IEEE)

[1]Department of Electrical Engineering, Govind Ballabh Pant Institute of Engineering and Technology, Pauri Garhwal, Uttarakhand 246194, India
[2]Department of Electrical Engineering, Indian Institute of Technology Patna (IIT Patna), Patna 801103, India
[3]Advanced Power and Energy Center, Department of Electrical Engineering and Computer Science, Khalifa University, Abu Dhabi, United Arab Emirates
[4]Department of Electrical and Electronics Engineering, Avanthi Institute of Engineering and Technology, Visakhapatanam 531113, India

Corresponding author: Utkal Ranjan Muduli (utkal.muduli@ku.ac.ae)

This work was supported in part by the Ministry of Human Resource Development and Ministry of Power, Government of India, through IMPRINT, under Project 1-18/2015-TS-TS.I; in part by the Khalifa University under Award KKJRC-2019-Trans2; and in part by the Advanced Technology Research Council ASPIRE Virtual Research Institute (VRI) Program, Abu Dhabi, United Arab Emirates, under Award VRI20-07.

ABSTRACT A solar photovoltaic distribution static compensator (SPV-DSTATCOM) under partial shading condition (PSC) is studied using a single-stage, 3-phase grid-connected mode. Under PSC, the performance of the grid-connected SPV-DSTATCOM is studied, and issues such as active current sharing, reactive power control, and harmonic elimination are addressed. Rejection of DC offset with such PSC condition is an issue when using a conventional Proportional Resonant (PR) controller. As a result of this research, a new and improved PR (IPR)-based second-order generalized integrator (SOGI) has been developed that has unity gain at the fundamental frequency and greater DC offset rejection capability to address the PR controller shortcomings. The proposed controller's performance is evaluated in both steady-state and dynamic conditions with varying loads and different PSC conditions. An experimental evaluation of the proposed controller's design assumptions is also presented in the form of a comparison with both the PR controller and the adaptive PR controller.

INDEX TERMS Reactive power supply, partial shading condition, proportional resonant controller, power system harmonics, second-order generalized integrator.

I. INTRODUCTION

In the last few years, increasing focus has been given towards Renewable Energy (RE) generation because of the perishable nature of fossil fuels, the growth of emission rates and the major issue of global warming. The introduction of renewable energy sources is capable of immediately satisfying the growing demand for energy [1]. Decentralized energy generation through RE sources possesses several distinct attributes compared to traditional sources of energy production. Hence, multidisciplinary research activities have been conducted to improve the available power conversion techniques along with the introduction of brand-new techniques regarding novel configuration, topologies, and control mechanisms. Considerable importance is given to the extensive use of solar photovoltaic cells in connection with grid situations due to the adverse effects of green house gas, global warming, and security along with the repayment period [2].

The use of solar photovoltaic systems (SPVs) is largely dependent upon the fluctuation in solar radiation along with the intensity of disturbances that occur in the grid. In the event of a particular grid initialization, large amounts

The associate editor coordinating the review of this manuscript and approving it for publication was S. K. Panda.

of photovoltaic panels are attached to the power grid. Concerning these systems, Partial Shading Condition (PSC) arises because of the shadow of either trees or buildings or due to moving clouds. In such a situation, the power vs. voltage curve seems more complex because of the emergence of numerous local maximum power points (MPPs). Out of these local maximum power points, one peak MPP illustrates the global MPP (GMPP). Traditional methods become inefficient in accurately tracking GMPP and can be erroneous in tracking any local MPP, resulting in a significant decrease in energy production and efficiency. New research articles demonstrate the importance of tracking GMPP in the case of rapid change in irradiance scenarios [3]–[5]. Therefore, the most important feature of the grid-connected photovoltaic system is to generate the optimal amount of power according to changing solar radiation. In this paper, one of the most important aspects for researchers is determining the global maximum under partial shading conditions. Some recent studies include bidirectional DPP fly back converters [6], Levy flight (JAYA-LF) based JAYA algorithm [7], flying squirrel search optimization (FSSO) [8], a spline-MPPT technique [9], PSO based method [10].These methodologies have trade-offs between fast tracking and accuracy of GMPP. One of the most advanced methodologies called Extreme Seeking Algorithm (ESA) [11] is employed in this paper for its better performance in tracking the GMPP.

Concerning a grid-tied PV system, a small amount of fluctuation in the voltage of the inverter output, as well as the grid voltage at the point of common coupling (PCC), can result in a much larger amount of inrush current within the system. Hence, a customized control mechanism is needed in case of grid synchronization. PLL is highly recommended by researchers to meet the above requirements [12]. Moreover, the phase-locked loop is also entitled to several limitations such as the non-linear property, complex tuning system, and slack, as well as diminishing outcomes in case of fragile grid conditions [13], [14]. To address these drawbacks, various innovative modern tuning mechanisms are suggested in the article [15]–[17]. The above-mentioned innovative tuning models compete with computational burden, system stability, system's dynamic response, enhanced system performance like sharing of active current in case of the existence of two different resources, issues regarding the quality of power, compensation of reactive power, harmonic elimination, improvement of grid current as well as grid voltage in terms of Total Harmonic Distortion (THD). However, these advanced tuning mechanisms again result in complex control measures that minimize the system's dynamic performance.

The primary objective of the grid-integrated SPV-DSTATCOM is to feed active and reactive power within the system in the presence of solar radiation [18], [19]. Apart from that, without solar radiation, this injects the harmonic compensation power needed by the load named DSTATCOM. It becomes very essential to maintain the harmonic-free, sinusoidal, steady, and unity power factor operation of the grid by using voltage control. Current regulation action is carried out via the hysteresis current regulator, linear PI regulator, or predictive regulator. This type of regulator is again classified as a synchronous rotating dq frame as well as a stationary reference frame. However, the 3-phase synchronous reference frame regulator yields undesirable results, since this requires data on the phase angle with respect to the rotating frame. The regulator performs erroneously when the phase angle evaluation becomes inaccurate. However, during the same time period, a stationary frame regulator outcome known as proportional resonance (PR) controller yields desirable results [20]. PR controller is used in the case of active power filter, PV systems, wind turbines, control rectifiers, induction motor (IM) drives and fuel cell operations [21]–[26]. Merits of PR controller involve 1) rapid dynamic response accompanied by zero steady state fault, 2) relatively less computational load since this does not need data on $\alpha\beta$ frame, 3) free from phase locked loop. However, it needs an appropriate synchronization technique with respect to grid-connected implementations [27], [28]. Deriving a high gain at resonance frequency is one of the major demerit points of the PR controller. The undesirable peak leads to a faulty evaluation with respect to the usual PR controller. As a consequence, this results in a sizable loss of performance. In addition to that, the existence of 2 unifiers/harmonizers is responsible for the fluctuation of the voltage frequency during the time where the unbounded gain is obtained taking into account the anticipated resonant frequency because of the dislocation of the resonant pole. It is demonstrated in terms of a significant steady state fault [29]. An APR regulator is introduced to address this issue of steady state error [30]. This proposes a fourth-order band pass filter along with an adaptive integration technique to track the deviation in grid frequency. As a result, this minimizes the frequency sensitivity. However, this creates more complications and puts more computational load on the system. As a consequence, the measured frequency becomes inaccurate due to the existence of a DC offset. It leads to the superposition of the low-frequency component on the basis of the mean value of the calculated frequency. Existence of DC offsets gives rise to both fundamental frequency variations and DC injection through grid-connected converters. Eliminating such variations becomes a burden due to its low-frequency characteristic [31]. Therefore, the international standard IEC 61727 has proposed a check of the DC offset limits in the case of PV connected to the grid less than 1% of its rated output current [32]. Such limitations reveal the significance of the decreasing DC offset prevailing within the input signal of the regulator.

The following points summarize the contributions of this paper.

- An advanced PR controller built upon the SOGI (IPR-SOGI) is proposed to address the issues concerning both high gains with phase jump and DC offsets present in the input signal.

- A method to generate a positive sequence input signal is adopted in the proposed controller using the proposed IPR-SOGI. This can be utilized in more ways for unit template generation and sequence load current extraction.
- The proposed controller is simple to implement, with a lower computational burden and a better dynamic response compared to various complex algorithms. It has a greater DC offset rejection capability; the greater harmonic reduction potential, meanwhile, increases the stability of the system.
- The performance of the proposed controller is confirmed under partial shading conditions accompanied by several distinct loading scenarios alongside dynamic conditions.
- Excellent results are obtained through a comparison of the experimental performance of the conventional PR controller with the proposed IPR-SOGI based controller.

The following five sections make up this document: the system topology and the control architecture of the improved PR controller are described in Section II, and the experimental validation and results with other control structures are discussed in Section III of the article. Section IV extends the conclusion.

II. PROPOSED IPR-SOGI METHOD FOR DSTATCOM CONTROL

A. SYSTEM DESCRIPTION

Devices such as static synchronous compensator (STATCOM) are used to regulate alternating-current energy transmission networks, such as the North American Electric Reliability Corporation (NERC). Using an electronic voltage source converter (VSC), it can provide or sink reactive alternating current (AC) power from a grid. As a fast-compensating reactive power source, distributed STATCOM (DSTATCOM) reduces voltage changes such as sags, surges, and flicker produced by the rapid change in reactive power demand in the transmission or distribution system [33]. Because a DC capacitor on the DC side of the VSC is used to maintain the DC link voltage constant, a DSTATCOM has a low active power generation capacity. A suitable energy storage device can be connected across the DC capacitor to boost its active power capability. Therefore, a solar photovoltaic array is connected on the DC side of DSTATCOM to produce an SPV-DSTATCOM structure, as illustrated in Fig. 1. Now, SPV-DSTATCOM has the ability to supply active and reactive power to the utility grid with greater reliability. The amount of active power generated depends on the solar irradiance and the panel temperature, wherever the reactive power generation completely depends on the amplitude of the grid voltage. This is because the reactive power demand from the load connected at the point of common coupling (PCC) regulates the grid voltage. The more inductive the load, the higher the reactive power demand at the PCC point, reducing the grid voltage at the PCC point.

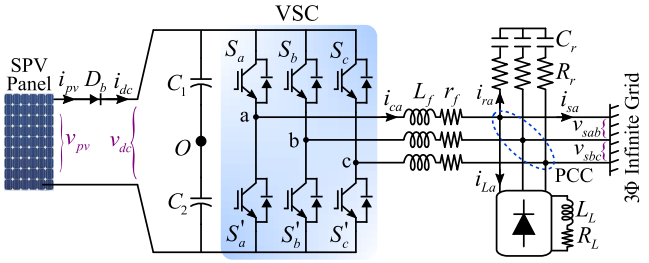

FIGURE 1. Configuration of grid integrated SPV-DSTATCOM.

If the DC link capacitor is utilized for this compensation, it can support reactive power for a period of few (2 to 3) cycles. The higher the DC-link capacitance, the longer the duration (only for transient period) for which the DC-link capacitor can release the stored energy in the form of reactive power to the grid. As the DC link voltage is supported by the PV system, it is most likely that the DC link can support the reactive power to the local load at PCC to stabilize the PCC voltage to some extent (up to the rated value of the PV VSC system). SPV-DSTATCOM generates an appropriate compensating reactive current through the line filter during injection or absorption of reactive power. DSTATCOM can deliver reactive power when the AC side voltage (v_i) of VSC is greater than the PCC voltage (v_s); on the other hand, DSTATCOM absorbs reactive power when v_s is greater than v_i. Regardless of the direction of the reactive current, the VSC operates in buck mode and the DC link voltage (v_{dc}) should always be greater than the peak of the line-to-line AC side voltage of the inverter. The line filter between the VSC and PCC, as shown in Figure 1, plays an important role here for the reactive power transfer. The line filter (L_f with parasitic resistance r_f) in PCC is also used to filter out high-frequency ripples in phase current. Line filter inductance can be calculated according to the relation (1).

$$L_f = \frac{(v_i - v_g)v_g}{2v_i f_{sw}(HB)} \tag{1}$$

where HB is the selected hysteresis band and f_{sw} is the switching frequency of VSC. Again, the ripple filter (that is, the series connected resistor R_r and a capacitor C_r) is used to eliminate the noise from the voltage signals. The ripple filter is designed so that it offers very high impedance at the fundamental frequency and low impedance to the switching frequency component. To satisfy this condition, $R_r C_r \ll T_s$ holds good. Considering $R_r C_r = T_s/4$ at a switching frequency of $f_{sw} = 10kHz$ $(1/T_s)$, the capacitor value is calculated as $C_r = 4.2\mu F \approx 10\mu F$ (based on availability) with $R_r = 6\,\Omega$. To analyze the SPV-DSTATCOM behavior at PCC, a three-phase alternating current main is connected to the three-phase non-linear load. The non-linear load is created by combining an unregulated diode bridge rectifier with a series of RL loads. The voltage and current sensors are used to measure the PCC line-to-line voltage, photovoltaic voltage and current, load, and grid side phase currents.

B. PROPOSED IPR-SOGI

Considering the sinusoidal input signal $v_s = V_{sm}\sin(\omega_s t + \phi_v)$, the magnitude step response of an ideal generalized integrator (GI) can be represented as (2). Here, V_{sm}, ω_s and ϕ_v are the maximum amplitude, angular frequency, and phase angle of the input signal, respectively.

$$v_{\alpha 1} = V_{sm}\left(1 - e^{-k_a t}\right)\sin(\omega_s t + \phi_v) \tag{2}$$

where $v_{\alpha 1}$ and $v_{\beta 1}$ are the closed-loop response of GI and its quadrature component, respectively. k_α is a gain that depends on the settling time of the step response of GI. In the Laplace domain, $v_s \rightarrow v_s(s)$ and $v_{\alpha 1} \rightarrow v_{\alpha 1}(s)$ can be denoted as (3).

$$\begin{aligned} v_s(s) &= \frac{V_{sm}\omega_s\cos\phi_v}{s^2+\omega_s^2} + \frac{V_{sm}s\sin\phi_v}{s^2+\omega_s^2} \\ v_{\alpha 1}(s) &= \frac{V_{sm}\omega_s\cos\phi_v}{s^2+\omega_s^2} + \frac{V_{sm}s\sin\phi_v}{s^2+\omega_s^2} \\ &\quad - \frac{V_{sm}k_\alpha(\cos\phi_v + \sin\phi_v) + V_{sm}s\sin\phi_v}{(s+k_\alpha)^2+\omega_s^2} \end{aligned} \tag{3}$$

Now, the open-loop transfer function of the GI with unit feedback can be obtained as (4).

$$G(s) = \frac{k_\alpha s}{s^2+\omega_s^2} + \frac{k_\alpha\omega_s}{s^2+\omega_s^2}\left(\frac{-\omega_s\sin\phi_v + (s+k_\alpha)\cos\phi_v}{\omega_s\cos\phi_v + (s+k_\alpha)\sin\phi_v}\right) \tag{4}$$

The open-loop transfer function in (4) contains a second-order denominator; hence, GI is further considered as second-order GI (SOGI). Under practical conditions, it is difficult to distinguish the initial phase of the input signal v_s; thus ϕ_v is considered as zero. Now, the expression for the SOGI open-loop transfer function ($G(s)$) can be reconfigured as (5).

$$G(s) = \frac{2k_\alpha s + k_\alpha^2}{s^2+\omega_s^2} = \underbrace{\left(1 + \frac{k_\alpha}{2s}\right)}_{G_1(s)}\underbrace{\left(\frac{2k_\alpha}{\omega_s}\right)}_{G_2(s)}\underbrace{\left(\frac{\omega_s/s}{1+(\omega_s/s)^2}\right)}_{G_3(s)} \tag{5}$$

where $G_1(s)$, $G_2(s)$ and $G_3(s)$ are sub transfer functions of $G(s)$. The transfer function $G(s)$ with unit feedback provides the closed transfer function as mentioned in (6).

$$G_{\alpha 1}(s) = \frac{G(s)}{1+G(s)} \tag{6}$$

With the grid voltage signal as input to $G_{\alpha 1}(s)$, variations in the impedance of the system lead to the possibility of resonance, resulting in competent controller reliability. To avoid such a scenario, another PR term should be added in $G(s)$. This modification can be achieved by changing the loop gain of $G_3(s)$ in its feedback path. Let $H_\beta(s)$ be the feedback path in $G_3(s)$ and can be denoted as (7).

$$H_\beta(s) = 1 + \frac{\omega_s}{s} + k_\beta\left(1 + \left(\frac{\omega_s}{s}\right)^2\right) \tag{7}$$

where k_β is introduced as an additional gain in the feedback path. Now, $G_3(s)$ can be modified to (8).

$$G_3(s) = \frac{\omega_s/s}{1+(\omega_s/s)H_\beta(s)} \tag{8}$$

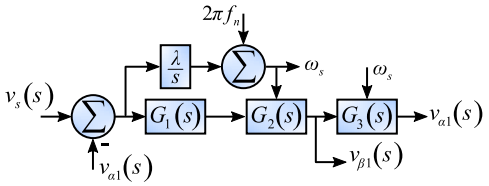

FIGURE 2. Block diagram of IPR-SOGI with original and quadrature generation.

Taking into account $G_3(s)$ in (5), the overall transfer function $G_{\alpha 1}(s)$ and $G_{\beta 1}(s)$ of the proposed IPR-SOGI can be derived as (9)-(10), respectively.

$$\begin{aligned} G_{\alpha 1}(s) &= \frac{v_{\alpha 1}(s)}{v_s(s)} \\ &= \frac{2k_\alpha s^2 + k_\alpha^2 s}{s^3 + (2k_\alpha + k_\beta\omega_s + \omega_s)s^2 + (\omega_s^2 + k_\alpha^2)s + k_\beta\omega_s^3} \end{aligned} \tag{9}$$

$$\begin{aligned} G_{\beta 1}(s) &= \frac{v_{\beta 1}(s)}{v_s(s)} \\ &= \frac{2k_\alpha\omega_s s + k_\alpha^2\omega_s}{s^3 + (2k_\alpha + k_\beta\omega_s + \omega_s)s^2 + (\omega_s^2 + k_\alpha^2)s + k_\beta\omega_s^3} \end{aligned} \tag{10}$$

Fig. 2 shows the block diagram to generate $v_{\alpha 1}(s)$ and $v_{\beta 1}(s)$, respectively, from $v_s(s)$. Here, the deviation in the angular frequency of the grid ($2\pi\Delta f_s$) can be calculated by integrating the error generated from $v_s(s) - v_{\alpha 1}(s)$ with the gain λ. ω_s can be further generated by adding $2\pi\Delta f_s$ with the nominal grid angular frequency ($2\pi f_n$). The estimated value of ω_s is utilized to evaluate the transfer functions $G_2(s)$ and $G_3(s)$. As a modified PR controller is utilized in the SOGI, this concept is further classified as IPR-SOGI. IPR-SOGI is capable of generating the original signal with its quadrature component with better dynamics and is completely dependent on the selection of the gains k_α and k_β. Optimal selection of these gains is possible through representation of the bode and root locus of the transfer function $G_{\alpha 1}(s)$ and $G_{\beta 1}(s)$, which is illustrated in Figs. 3(a) and 3(b), respectively. It can be seen that the phase margin and the gain margin are positive, indicating that the system is running smoothly when k_α=2500 and k_β=500. It is also possible to design the parameters k_α and k_β from the time domain analysis according to the following procedure.

Step 1: Select the settling time t_s for the IPR-SOGI controller.

Step 2: Set the damping ratio ζ to 0.707 for low overshoot and shorter settling time.

Step 3: Determine the angular frequency of the natural oscillation ω_n as (11).

$$\omega_n = \frac{4.4}{\zeta t_s} \tag{11}$$

Step 4: Consider the characteristic equation as $1 + G(s) = (s+c)(s+2\zeta\omega_n s + \omega_n^2)$, where the variable c should

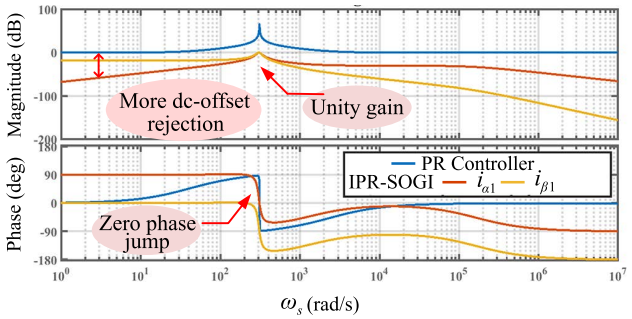

(a) Comparative study of IPR-SOGI with conventional PR based SOGI

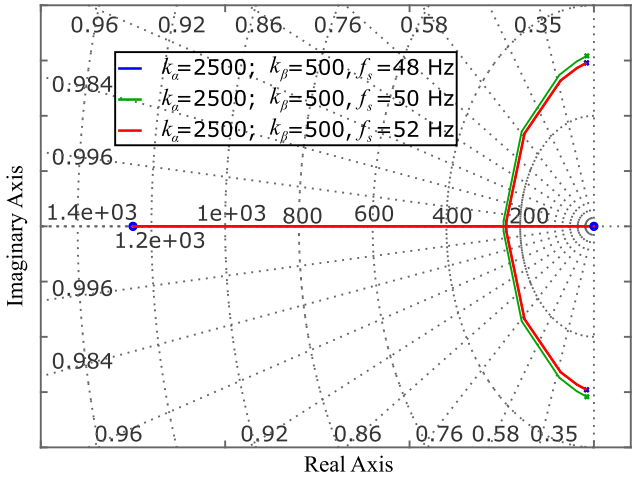

(b) Root locus analysis with system frequency variation

FIGURE 3. Stability analysis through root locus and frequency response.

satisfy $c > G_d\zeta\omega_n$ with $G_d > 5$ for an optimum transient response. Now, the controller gains k_α and k_β can be obtained as (12).

$$k_\beta = \frac{G_d\zeta\omega_n^3}{\omega_s^3}$$
$$k_\alpha = \frac{1}{2}\left((1+G_d)\zeta\omega_n - \omega_s(1+k_\beta)\right) \quad (12)$$

Compared to the proportional resonant (PR) controller, the analysis corresponding to the proposed IPR-SOGI revealed that the suggested controller performs as a band-pass filter and has better DC offset discarding ability. However, the PR controller acts as a notch filter and has a flat characteristic on the magnitude plot. Furthermore, when compared to a traditional PR controller, this suggested IPR-SOGI controller produces a zero phase jump. The robustness of this proposed controller interacts negatively with the fluctuation in grid frequency in transitory scenarios, as illustrated in Fig. 3(b).

C. MPPT CONTROL ALGORITHM

An improved ESA has been implemented to track the GMPP from the PV curve of non-linear characteristics, as shown in Fig. 4. It is efficient under fast and persistent changes in solar irradiance, overcoming disturbances and uncertainties. The perturbed power and the perturbed current contain significant ripples. To filter out these ripples, two High

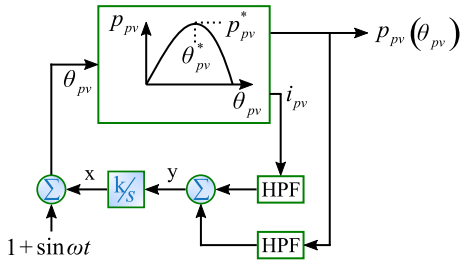

FIGURE 4. Block diagram of improved ESA algorithm.

Pass Filters (HPFs) having cutoff frequency of 100 Hz are introduced. The outputs of these HPFs are added together and are termed the demodulated signal (y). The demodulated signal is integrated and multiplied with a small value of $k = 0.2$ to generate the adaptive signal (x). Here, a perturbation signal $(1+\sin\omega t)$ is added to the input adaptive signal (x), which results in the maximum output power and can adaptively bind the GMPP. Moreover, the improved ESA is an adaptive controller and does not require fine-tuning for better performance.

D. SPV-DSTATCOM CONTROL ARCHITECTURE

The SPV-DSTATCOM control architecture includes the extraction of the positive sequence voltage, as well as their quadrature elements via the IPR-SOGI control mechanism. Furthermore, such elements are used to evaluate unit templates for grid synchronization. Then this proposed control framework is used to evaluate the fundamental components of the load current that are used to measure the reference current with respect to the hysteresis current controller to generate gate pulses for grid-tied inverters.

1) UNIT TEMPLATE GENERATION

Initially, two voltage sensors are used in the PCC to measure the line voltage between phases a-b (v_{sab}) and phases b-c (v_{sbc}). The phase voltages at the PCC are then estimated using (13).

$$v_{sa} = \frac{2v_{sab} + v_{sbc}}{3}$$
$$v_{sb} = \frac{-v_{sab} + v_{sbc}}{3}$$
$$v_{sc} = \frac{-v_{sab} - 2v_{sbc}}{3} \quad (13)$$

Subsequently, the phase voltages of the PCC in *abc*-frame (v_{sa}, v_{sb}, v_{sc}) can be transformed to the stationary $\alpha\beta$-frame ($v_{s\alpha\beta}$) using (14) to perform IPR-SOGI.

$$v_{s\alpha\beta} = \frac{2}{3}\left[1 \;\; a \;\; a^2\right]\left[v_{sa} \;\; v_{sb} \;\; v_{sc}\right]^T \quad (14)$$

Here, $v_{s\alpha} = \Re\left(v_{s\alpha\beta}\right)$ and $v_{s\beta} = \Im\left(v_{s\alpha\beta}\right)$ represent the voltage on the α-axis and the β-axis, respectively. $v_{s\alpha}$ ($v_{s\beta}$) is given as input to the IPR-SOGI, while $v_{\alpha1}$ and $v_{\beta1}$ ($v_{\alpha2}$ and $v_{\beta2}$) are taken as output from the IPR-SOGI. The flow diagram of the corresponding conversion procedure is shown

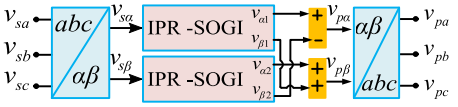

FIGURE 5. Positive sequence generator using IPR-SOGI.

in Fig. 5. The estimation of the positive sequence voltage in $\alpha\beta$-frame from these output quantities is computed as per (15).

$$v_{p\alpha} = v_{\alpha 1} - v_{\beta 2} \quad v_{p\beta} = v_{\alpha 2} + v_{\beta 1} \tag{15}$$

Using $\alpha\beta$-to-abc frame conversion, the positive sequence voltage in abc-frame (v_{pa}, v_{pb}, v_{pc}) can be calculated as using (16).

$$\begin{bmatrix} v_{pa} \\ v_{pb} \\ v_{pc} \end{bmatrix} = \begin{bmatrix} 1 & 0 \\ \cos(2\pi/3) & \sin(2\pi/3) \\ \cos(4\pi/3) & \sin(4\pi/3) \end{bmatrix} \begin{bmatrix} v_{p\alpha} \\ v_{p\beta} \end{bmatrix} \tag{16}$$

Furthermore, the three-phase unit template (u_{pa}, u_{pb}, u_{pc}) can be derived as (17) from the positive sequence phase voltage.

$$u_{pa} = v_{pa}\frac{1}{v_t} \qquad u_{pb} = v_{pb}\frac{1}{v_t} \qquad u_{pc} = v_{pc}\frac{1}{v_t} \tag{17}$$

where $v_t = \sqrt{\frac{2}{3}\left(u_{pa}^2 + u_{pb}^2 + u_{pc}^2\right)}$ represents the amplitude of the terminal voltage. Equation (17) can also be used to estimate the quadrature unit template (u_{qa}, u_{qb}, u_{qc}) in (18).

$$\begin{aligned} u_{qa} &= 0.577(u_{pc} - u_{pb}) \\ u_{qb} &= 0.288(3u_{pa} + u_{pb} - u_{pc}) \\ u_{qc} &= 0.288(-3u_{pa} + u_{pb} - u_{pc}) \end{aligned} \tag{18}$$

These measured positive sequence unit templates in conjunction with the quadrature unit templates are used to generate the fundamental positive sequence, as well as the quadrature element of the load current, as discussed in the following section.

2) LOAD CURRENT COMPONENT EXTRACTION

The estimated 3-phase load current consists of a fundamental component, a harmonic component, and a quadrature component. The fundamental component represents the active power, whereas the quadrature component represents the reactive power. First, the fundamental positive sequence components of the load current of the corresponding phases are measured using the procedure shown in Fig. 5. Furthermore, the fundamental elements of the load current are utilized to measure the reference currents in relation to SPV-DSTATCOM. Fig. 6 shows the fundamental component estimation process using the proposed IPR-SOGI algorithm. These measured fundamental components are passed through the sample, followed by a hold circuit and a zero-crossing detector (ZCD). Within each phase, two distinct ZCDs are used to generate $\hbar_{px}$ or $\hbar_{qx}$, $x \in \{a, b, c\}$. The unit template, i.e., u_{px} (u_{qx}) is used to activate the ZCD with respect to $\hbar_{px}$

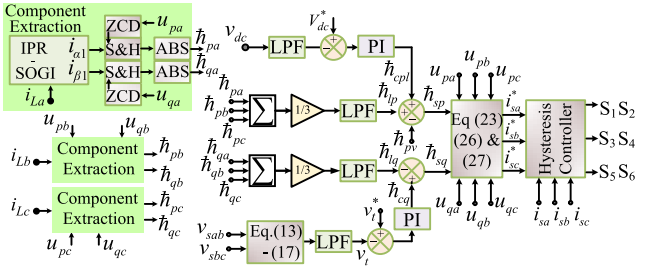

FIGURE 6. SPV-DSTATCOM overall control structure for switching pulse generation.

($\hbar_{px}$). In this case, Equation (19) calculates the mean value of the direct (h_{lp}) and quadrature (h_{lq}) components, respectively.

$$\hbar_{lpa} = \frac{1}{3}\sum_x \hbar_{px} \quad \text{and} \quad \hbar_{lqa} = \frac{1}{3}\sum_x \hbar_{qx} \tag{19}$$

3) LOSS TERM ESTIMATION

Surplus current is extracted from the grid to keep the actual voltage of the DC link capacitor (v_{dc}) within its reference value ((V_{dc}^*)) when the SPV-DSTATCOM is operating. This maintains the DC link voltage at its reference voltage during transitory periods of charging and discharging. Surplus currents, on the other hand, are usually in phase with the grid voltage, resulting in additional losses if the system is operated. The difference between the reference DC link voltage and the actual DC link voltage is regarded as the DC link voltage error and is provided within the proportional integral (PI) controller to calculate the current with regard to the additional power losses. In this case, Equation (20) represents the discrete-time implementation of the PI controller to determine the loss component $\hbar_{cpl}^{(k)}$.

$$\hbar_{cpl}^{(k)} = \hbar_{cpl}^{(k-1)} + k_{p1}[v_{err}^{(k)} - v_{err}^{(k-1)}] + k_{i1}v_{err}^{(k)} \tag{20}$$

where k_{p1} and k_{i1} represent the PI gains and are tabulated in Table 1. k denotes the present sample of the controller. The DC link error voltage is represented by $v_{err}^{(k)} = V_{dc}^* - v_{dc}^{(k)}$ with V_{dc}^* calculated from the GMPP of the ESA algorithm.

4) REFERENCE CURRENT FORMATION

For the reference current generation, the current component corresponding to active and reactive power generation along with the loss components must be estimated and summarized as in Fig. 6. PV current (i_{pv}) and the PV voltage (v_{pv}) are initially measured through suitable sensors and supplied to the MPPT mentioned in [11]. Using the ESA MPPT algorithm, V_{dc}^* is generated by appropriate selection of step size. The current supplied from PV can be estimated from the PV power ($p_{pv} = i_{pv}v_{pv}$) and the terminal voltage v_t as mentioned in (21).

$$\hbar_{pv} = \frac{2}{3}\frac{i_{pv}v_{pv}}{v_t} \tag{21}$$

The effective component of the load current $\hbar_{sp}$ is calculated from the loss component, as well as the average load active

component provided by the grid, and can be estimated by (22).

$$\hbar_{sp} = \hbar_{lpa} + \hbar_{cpl} - \hbar_{pv} \tag{22}$$

The fundamental reference currents are obtained by multiplying the subsequent component by its respective unit template, which is represented in (23).

$$i^*_{pa} = \hbar_{sp} U_{pa} \qquad i^*_{pb} = \hbar_{sp} U_{pb} \quad i^*_{pc} = \hbar_{sp} U_{pc} \tag{23}$$

Similarly, the quadrature component of the load current is obtained by measuring $\hbar_{sq}$, i.e., the reactive weight component. The corresponding reactive weight component is calculated by subtracting the average reactive weight of the fundamental component from the estimated reactive weight of the AC component by (24).

$$\hbar_{sq} = \hbar_{cq} - \hbar_{lqa} \tag{24}$$

Concerning ZVR, the reactive reference current is obtained from the voltage control loop in addition to the proportional integral controller output, as shown in (25).

$$\hbar^{(k)}_{cq} = \hbar^{(k-1)}_{cq} + k_{p2}[v^{(k)}_{t,err} - v^{(k-1)}_{t,err}] + k_{i2} v^{(k)}_{t,err} \tag{25}$$

where $v_{t,err}(i) = v^*_t(i) - v_t(i)$ represents the terminal voltage error. $v^*_t(i)$ is the reference terminal voltage. k_{p2} and k_{i2} symbolize PI gains and are tabulated in Table 1. Equation (26) is used to calculate the reactive weight component in relation to the load current.

$$i^*_{qa} = U_{qa}\hbar_{sq} \quad i^*_{qb} = U_{qb}\hbar_{sq} \quad i^*_{qc} = U_{qc}\hbar_{sq} \tag{26}$$

Finally, Equation (27) calculated the reference grid current in relation to the hysteresis current controller.

$$i^*_{sa} = i^*_{pa} + i^*_{qa} \quad i^*_{sb} = i^*_{pb} + i^*_{qb} \quad i^*_{sc} = i^*_{pc} + i^*_{qc} \tag{27}$$

The reference current error can be generated here by subtracting the sensed grid currents (i_{sa}, i_{sb}, i_{sc}) from the grid reference currents ($i^*_{sa}, i^*_{sb}, i^*_{sc}$). Such errors are committed using a hysteresis current controller (HCC) to generate gate pulses that power the grid-connected inverter. The switching frequency (f_{sw}) of the VSC is regulated by the HCC hysteresis band (HB). To ensure that the resonant frequency (f_{res}) is not affected by the minimum switching frequency ($f_{sw,min}$), the frequency band is selected so that the maximum switching frequency ($f_{sw,max}$) does not exceed the calculated switching frequency limits of the insulated gate bipolar transistor (IGBT) switch [34]. VSC and filter design can be easily performed by establishing a switching frequency band as (28) [35].

$$10 f_s < f_{res} < f_{sw,min} < f_{sw,avg} < f_{sw,max} \tag{28}$$

where f_s represents the frequency of the grid. The maximum switching frequency, DC link voltage, and PCC grid voltage must be taken into account when determining the appropriate current hysteresis band for a three-phase VSC. In other words, the HB need not be extremely small or incredibly large in any way. The HCC tracking capability is also

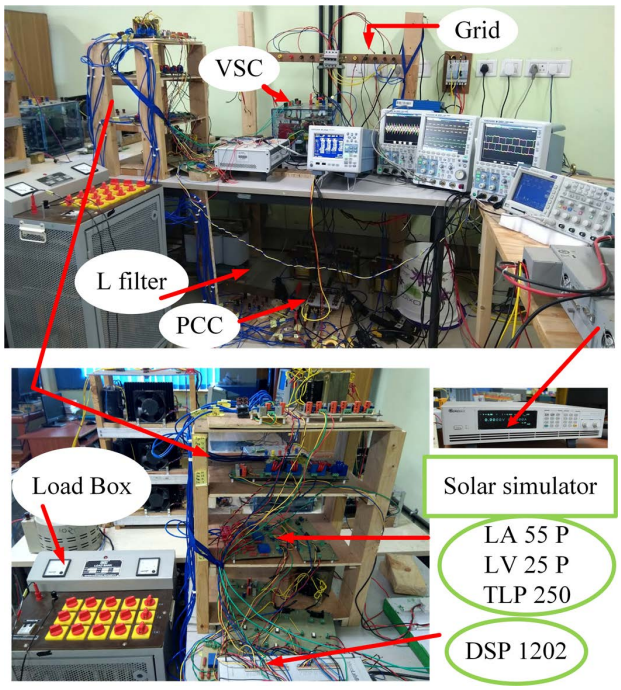

FIGURE 7. Experiment set-up developed at laboratory.

TABLE 1. Experimental set-up parameters.

System quantities	Values
Source voltage (rms)	60 V, 60 V, 60 V L-N, 50 Hz
Feeder impedance	R_s = 0.3 Ω, L_s = 0.03 mH, R_s /X_s = 3.185
Ripple filter	R_r = 6 Ω, C_r = 10 μF
nonlinear load	3-Φ rectifier with RL load of 4 Ω, 40 mH
Load power	$P_L = 565W$
Load current	7.4 A
PI tuning parameter	k_{p1} = 0.152, k_{i1} = 0.016, k_{p2} = 0.0136, k_{i2} = 0.0019
DSTATCOM parameter	V^*_{dc} = 107 V, C_{dc} = 2200 μF, L_f = 5 mH
PV emulator rating	P_{mpp} = 1600 W, V_{GMPP} = 106.4 V, I_{GMPP} = 15.029 A, V_{oc} = 125.2 V, I_{sc} = 16.268 A

enhanced by the trade-off between the permissible injected PCC current % THD (within the IEEE-519 limit of 5%) and the average switching frequency ($f_{sw,avg}$). Consider I_i be the rated value of the injected current. A fixed-band hysteresis current regulation limit of between 5% of I_i ($0.05I_i$ A) in the ripple of the inverter side current is considered acceptable.

III. EXPERIMENTAL VERIFICATION

In the laboratory, an experimental test bench of grid-integrated SPV-DSTATCOM is designed and illustrated in Fig. 7. This test bench is used to validate the performance of the suggested control methodology and includes

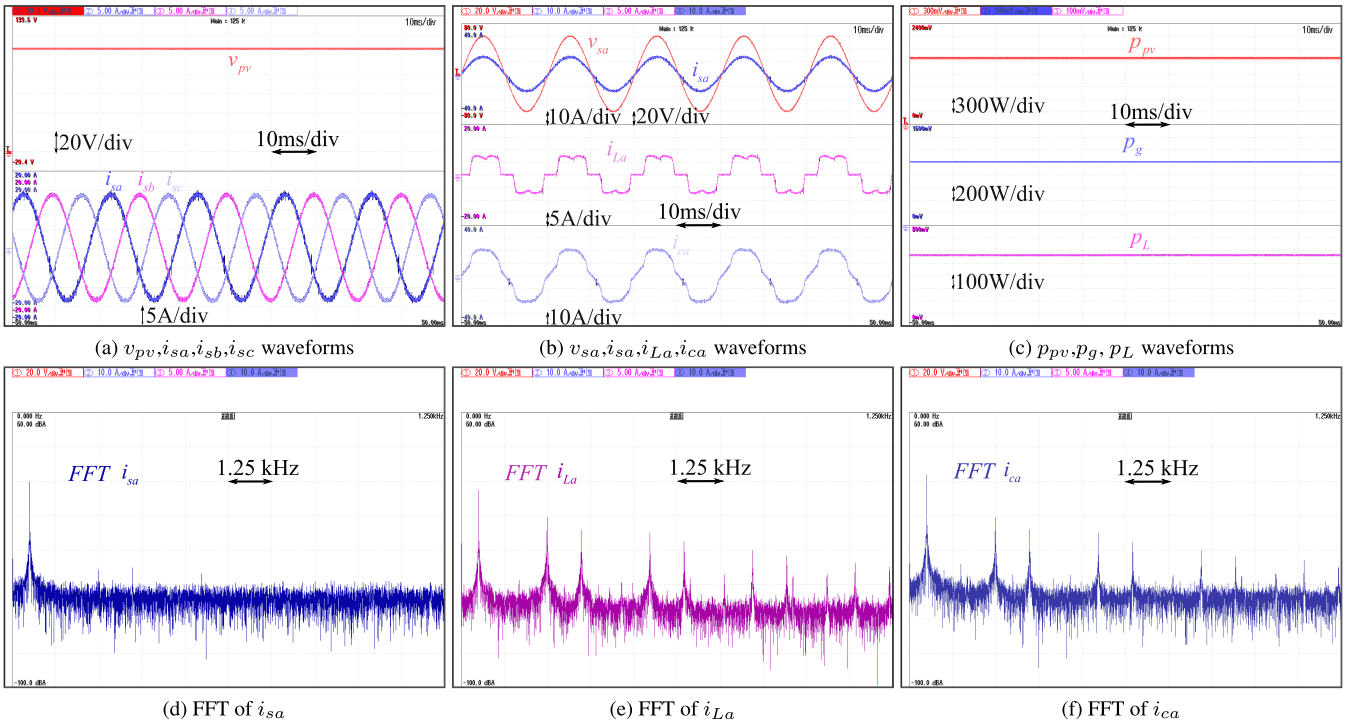

(a) v_{pv},i_{sa},i_{sb},i_{sc} waveforms (b) v_{sa},i_{sa},i_{La},i_{ca} waveforms (c) p_{pv},p_g, p_L waveforms

(d) FFT of i_{sa} (e) FFT of i_{La} (f) FFT of i_{ca}

FIGURE 8. Experimental verification of Grid tied SPV system with PSC under balance grid and balance non-linear loading.

a solar photovoltaic emulator (Chroma 62020H-150S), a 3-phase 2-level VSC (using 6 SEMIKRON SKM100 GB063D IGBT switches), interfacing inductors, a ripple filter, a 3-phase diode bridge rectifier, and a nonlinear R-L load. Table 1 shows the experimental test parameters for the grid-connected SPV-DTATCOM system. The voltage transducers (LEM LV 25P) and current transducers (LEM 55P) are used to measure the line voltage and current signals. Steady- and transient-state waveforms are recorded using a 4-channel YOKOGAWA WT500 power analyzer and a 4-channel YOKOGAWA DSO DCM2024 digital storage oscilloscope. The control mechanism is implemented using the dSPACE MicroLabBox DS1202. The pulses generated by the DS1202 are directed through the TLP-250 driver circuit to the VSC switches. Taking into account the computation time of the proposed controller, the sample time of DS1202 is set to 50 μs. At the time of the experiment, the DC link voltage follows the SPV voltage through the GMPP algorithm and V_{mpp} is maintained at 106.4 V for this test. In order to achieve various performance measurements, several test scenarios are implemented as described in the following subsections.

A. STEADY-STATE PERFORMANCE UNDER PSC

The test model is examined in the presence of partial shading in a balanced grid, as well as a nonlinear loading scenario. The shadow is created with the help of a solar emulator. It caused multiple jumps in current on the voltage curve with respect to SPV, as well as the formation of several local maximum power points along the power curve of solar photovoltaics. In the case of partial shading, the maximum solar photovoltaic voltage is 106.4 V and the maximum current is 15 A. In addition to that, the respective SPV has an efficiency rate of 99.78% in terms of available power, that is, 1596 W, indicating that the majority of the energy is generated by the PV array. Fig. 8(a) depicts the grid currents injected into the grid from VSC while the DC-link voltage is held constant at its reference value derived from the global maximum power point. Fig. 8(b) shows the phase voltage v_{sa}, grid current i_{sa}, compensation grid i_{ca}, load current i_{La} with respect to the grid. It can be seen that the compensation current of the VSC system provides the non-linear load requirements. Moreover, the grid current i_{sa} of SPV-STATCOM provides a sinusoidal current and maintains a unit power factor with respect to the grid voltage. Fig. 8(c) depicts the power flow for the entire system. It can be seen that PV power p_{pv}, grid power p_g and the load power p_L are 1.59 kW, 1.1 kW, and565 W, respectively. Figs. 8(d), (e) and (f) show the percentage of THD for i_{sa}, i_{ca} and i_{La}, respectively. It can be observed that % THD of i_{sa}, i_{ca} and i_{La} are 1.68%, 9.74% and 26.24%, respectively. The THD of the injected grid current is maintained within the 5% limit according to IEEE Standard 519-2014.

B. TRANSIENT STATE PERFORMANCE WITH UNBALANCE LOADING UNDER PSC

Figs. 9(a)-(c) show the dynamic performance of the SPV-DSTATCOM system when the b-phase load is perturbed. Due to the declination of the b-phase load, the net

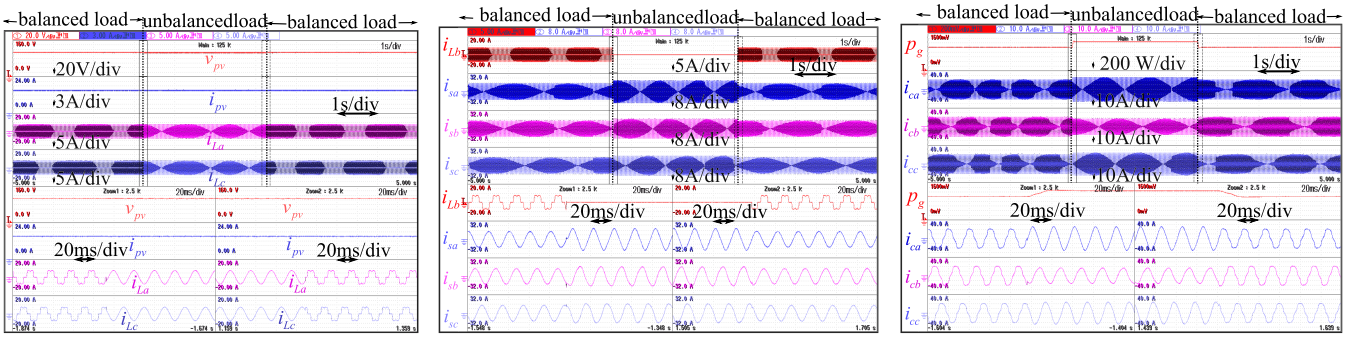

(a) v_{pv},i_{pv},i_{La},i_{Lc} waveforms (b) i_{Lb},i_{sa},i_{sb},i_{sc} waveforms (c) p_g,i_{ca},i_{cb},i_{cc} waveforms

FIGURE 9. Experimental performance evaluation during load perturbation considering partial shading condition.

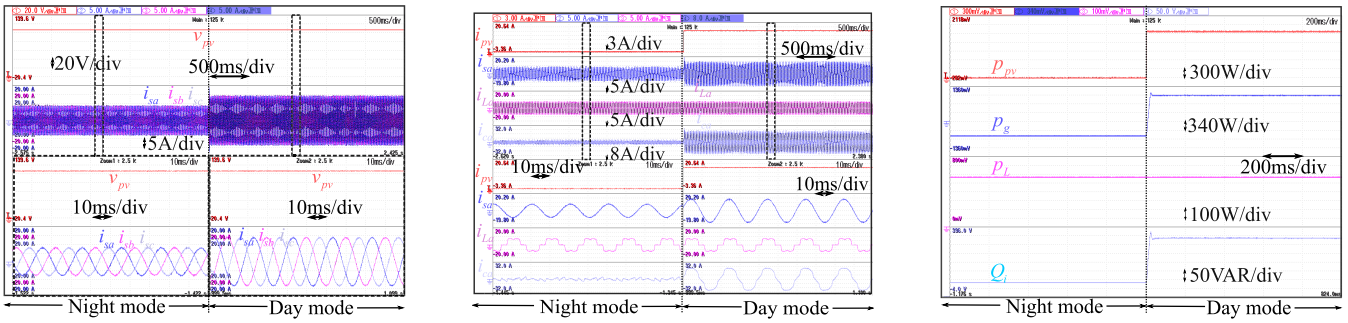

(a) v_{pv},i_{sa},i_{sb},i_{sc} waveforms (b) i_{pv},i_{sa},i_{sb},i_{ca} waveforms (c) p_{pv},p_g,p_L,Q_i waveforms

FIGURE 10. Experimental results: Dynamic condition analysis under PSC with changeover from night mode to day mode.

demand for harmonic current begins to decline. However, there is no change observed in PV current (I_{pv}) and PV voltage (v_{pv}), as observed in Fig. 9(a). Moreover, v_{pv} is maintained in accordance with the reference voltage generated by global MPPT. At the instant of removal of the load, an increase in grid current (i_{sa}, i_{sb}, i_{sc}) is observed in Fig. 9(b). As a result, the grid power increases, as illustrated in Fig. 9(c). The dynamics of the VSC compensating currents (i_{ca}, i_{cb}, i_{cc}) are shown in Fig. 9(c), where the VSC current of phase-b is observed to be sinusoidal because it does not have to supply the harmonic current in phase-b.

C. NIGHT MODE TO DAY MODE

The operating procedure of SPV-DSTATCOM from night to day is shown in Fig. 10(a). Without solar radiation, the SPV-DSTATCOM system operates in the DSTATCOM mode using a 107 V DC-link voltage and a 0 A SPV current. In the presence of solar radiation, the SPV current increases from 0 A to 15 A while the DC link voltage remains constant at 107 V, while the magnitude of the grid current begins to increase, as shown in Fig. 10(b). The compensation current includes both the load current and the injected grid current during day mode. In Fig. 10(c), PV power P_{pv} is zero and maximum power during night and day mode conditions, respectively. The load power is constant during this scenario. The real power of the grid is negative during the night mode, which indicates that the power of the grid is delivered to the load and DC link capacitors. Here, Q_i indicates the reactive power injected by DSTATCOM at the point of common coupling.

D. SUDDEN CONNECTION OR DISCONNECTION OF THE NONLINEAR LOAD WITH SPV-DSTATCOM

The robustness of the proposed method is observed in SPV-DSTATCOM by instantaneous connection and disconnection of the nonlinear load at constant solar irradiation, as shown in Fig. 11. When a sudden disconnect (connection) of the load occurred, the current of the grid started to increase (decreasing), as shown in Fig. 11(a). Furthermore, the DC link voltage is maintained constant according to the reference value of the global MPPT during connecting or disconnecting the nonlinear load. It can be observed in Fig. 11(b) that the compensation current i_{ca} provides the load requirement during the loading condition. Currents i_{ca} and i_{sa} are equal in the no load state. In addition, the current and voltage of the grid are kept in phase, considering the operation of the unit power factor. The reactive power in the grid Q_g is nearly zero during connection or disconnection of the non-linear load, as shown in Fig. 11(c). However, the PV power remains constant during this period. The power injected into the grid is reduced during loading, as the available PV power is constant at constant solar irradiance. During inductive loading alone,

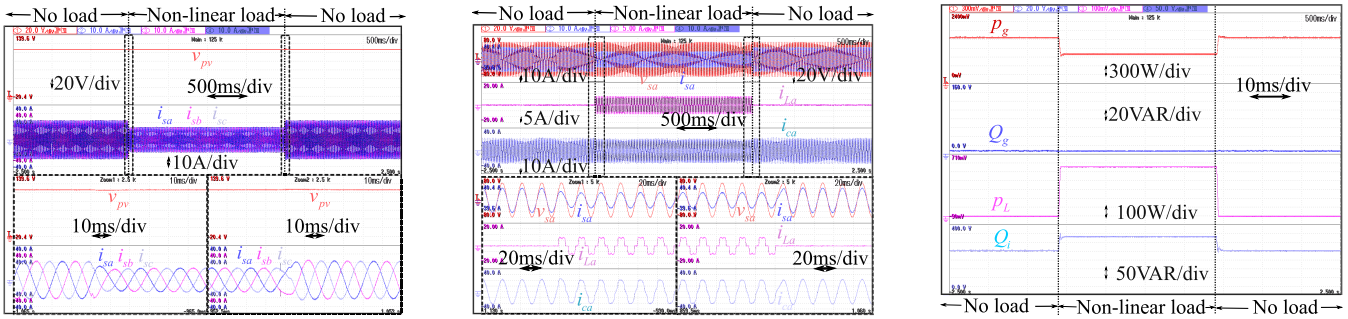

(a) v_{pv},i_{sa},i_{sb},i_{sc} waveforms (b) v_{sa},i_{sa},i_{La},i_{ca} waveforms (c) p_g,Q_g, p_L,Q_i waveforms

FIGURE 11. Dynamic condition analysis with PSC under sudden increment in load demand.

TABLE 2. Comparative Analysis for proposed IPR-SOGI.

Algorithm	Grid current THD	DC offset rejection	Steady state error	PSC	Computational complexity	DSP Speed	DC-link voltage ripple	Computation time	Requirement of cache memory
PR [36]	3.82%	no rejection	moderate	×	moderate	low	high	40 μs	high
DPR [37]	2.9%	less rejection capability	higher	×	comparatively higher	low	medium	50 μs	low
Proposed	3.1%	more rejection capability	lower	✓	lower	high	low	30 μs	low

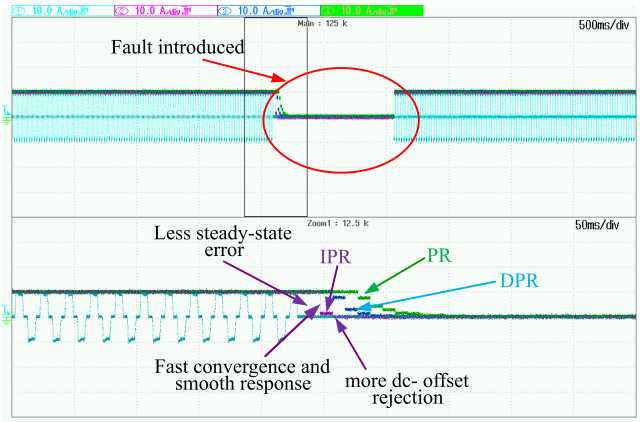

FIGURE 12. Dynamic response with Comparison performance of IPR-SOGI, PR and DPR.

the injected reactive power Q_i at PCC can be observed in Fig. 11(c).

E. COMPARISON RESULT

Fig. 12 depicts a comparative performance of the PR [36] and damped PR (DPR) [37] based controllers with the proposed IPR-SOGI controller. This comparative study considers performance indices such as the dynamic response of weight components during load withdrawal. It can be observed from Fig. 12 that the suggested controller has a faster convergence time and lower steady-state error. In addition to that, IPR-SOGI has a higher capability to eliminate dc offsets. Furthermore, Table 2 is provided to indicate indices such as %THD, steady-state error, PSC, computational complexity, fluctuation of DC link voltage, and cache memory requirement. It can be concluded that the proposed IPR perform better during partial shading conditions with lower computational burden.

IV. CONCLUSION

The real-time execution of the SPV-DSTATCOM system connected to the grid during partial shading conditions, with the aim of removing the DC offset, is demonstrated here. Through the use of the ESA, the accessible maximum power is generated from the SPV-DSTATCOM system with different transient scenarios. According to the findings of the preceding analysis for IPR-SOGI, the quality of the power generated by the grid is improved by unpredictable SPV power generation accompanied by unusual grid and load scenarios. Compared to the traditional proportional resonance controller, the IPR-SOGI method yields excellent results in terms of DC offset rejection and increased THD reduction potential, as well as increased system stability. Analytical investigations along with experimental validations are also performed in the laboratory for the SPV-DSTACOM with the proposed IPR-SOGI controller. It is found that the grid

current is injected with the desired power factor at a lower %THD than the permissible IEEE-519 limit.

REFERENCES

[1] W. Xiao, M. S. El Moursi, O. Khan, and D. Infield, "Review of grid-tied converter topologies used in photovoltaic systems," *IET Renew. Power Gener.*, vol. 10, no. 10, pp. 1543–1551, Nov. 2016.

[2] K. Wang, R. Zhu, C. Wei, F. Liu, X. Wu, and M. Liserre, "Cascaded multilevel converter topology for large-scale photovoltaic system with balanced operation," *IEEE Trans. Ind. Electron.*, vol. 66, no. 10, pp. 7694–7705, Oct. 2019.

[3] G. M. Madhu, C. Vyjayanthi, and C. N. Modi, "Investigation on effect of irradiance change in maximum power extraction from PV array interconnection schemes during partial shading conditions," *IEEE Access*, vol. 9, pp. 96995–97009, 2021.

[4] S. K. Cherukuri, B. P. Kumar, K. R. Kaniganti, S. Muthubalaji, G. Devadasu, T. S. Babu, and H. H. Alhelou, "A novel array configuration technique for improving the power output of the partial shaded photovoltaic system," *IEEE Access*, vol. 10, pp. 15056–15067, 2022.

[5] M. Kermadi, Z. Salam, A. M. Eltamaly, J. Ahmed, S. Mekhilef, C. Larbes, and E. M. Berkouk,, "Recent developments of MPPT techniques for PV systems under partial shading conditions: A critical review and performance evaluation," *IET Renew. Power Gener.*, vol. 14, no. 17, pp. 3401–3417, Dec. 2020.

[6] H. Jeong, S. Park, J.-H. Jung, T. Kim, A.-R. Kim, and K. A. Kim, "Segmented differential power processing converter unit and control algorithm for photovoltaic systems," *IEEE Trans. Power Electron.*, vol. 36, no. 7, pp. 7797–7809, Jul. 2021.

[7] R. Motamarri and N. Bhookya, "JAYA algorithm based on Lévy flight for global MPPT under partial shading in photovoltaic system," *IEEE J. Emerg. Sel. Topics Power Electron.*, vol. 9, no. 4, pp. 4979–4991, Aug. 2021.

[8] N. Singh, K. K. Gupta, S. K. Jain, N. K. Dewangan, and P. Bhatnagar, "A flying squirrel search optimization for MPPT under partial shaded photovoltaic system," *IEEE J. Emerg. Sel. Topics Power Electron.*, vol. 9, no. 4, pp. 4963–4978, Aug. 2020.

[9] A. Ostadrahimi and Y. Mahmoud, "Novel spline-MPPT technique for photovoltaic systems under uniform irradiance and partial shading conditions," *IEEE Trans. Sustain. Energy*, vol. 12, no. 1, pp. 524–532, Jan. 2020.

[10] S. Rajendran and H. Srinivasan, "Simplified accelerated particle swarm optimisation algorithm for efficient maximum power point tracking in partially shaded photovoltaic systems," *IET Renew. Power Gener.*, vol. 10, no. 9, pp. 1340–1347, Oct. 2016.

[11] Y. Liu, J. Wei, X. Zong, W. Yi, and R. Liu, "Research on maximum power point tracking based on extremum seeking algorithm," in *Proc. IEEE 4th Inf. Technol., Netw., Electron. Autom. Control Conf. (ITNEC)*, Jun. 2020, pp. 2502–2506.

[12] N. Hui, D. Wang, and Y. Li, "A novel hybrid filter-based PLL to eliminate effect of input harmonics and DC offset," *IEEE Access*, vol. 6, pp. 19762–19773, 2018.

[13] R. Ma, J. Li, J. Kurths, S.-J. Cheng, and M. Zhan, "Generalized swing equation and transient synchronous stability with PLL-based VSC," *IEEE Trans. Energy Convers.*, vol. 37, no. 2, pp. 1428–1441, Jun. 2021.

[14] M. A. Awal and I. Husain, "Unified virtual oscillator control for grid-forming and grid-following converters," *IEEE J. Emerg. Sel. Topics Power Electron.*, vol. 9, no. 4, pp. 4573–4586, Aug. 2021.

[15] M. Karimi-Ghartemani, S. A. Khajehoddin, P. K. Jain, A. Bakhshai, and M. Mojiri, "Addressing DC component in PLL and notch filter algorithms," *IEEE Trans. Power Electron.*, vol. 27, no. 1, pp. 78–86, Jan. 2011.

[16] B. Shakerighadi, E. Ebrahimzadeh, M. G. Taul, F. Blaabjerg, and C. L. Bak, "Modeling and adaptive design of the SRF-PLL: Nonlinear time-varying framework," *IEEE Access*, vol. 8, pp. 28635–28645, 2020.

[17] M. Mellouli, M. Hamouda, J. B. H. Slama, and K. Al-Haddad, "A third-order MAF based QT1-PLL that is robust against harmonically distorted grid voltage with frequency deviation," *IEEE Trans. Energy Convers.*, vol. 36, no. 3, pp. 1600–1613, Sep. 2021.

[18] A. Dash, D. P. Bagarty, P. K. Hota, R. K. Behera, U. R. Muduli, and K. Al Hosani, "DC-offset compensation for three-phase grid-tied SPV-DSTATCOM under partial shading condition with improved PR controller," *IEEE Access*, vol. 9, pp. 132215–132224, 2021.

[19] A. Dash, D. P. Bagarty, P. K. Hota, U. R. Muduli, K. A. Hosani, and R. K. Behera, "Performance evaluation of three-phase grid-tied SPV-DSTATCOM with DC-offset compensation under dynamic load condition," *IEEE Access*, vol. 9, pp. 161395–161406, 2021.

[20] N. Mohammed and M. Ciobotaru, "Adaptive power control strategy for smart droop-based grid-connected inverters," *IEEE Trans. Smart Grid*, vol. 13, no. 3, pp. 2075–2085, May 2022.

[21] B. W. Franca, M. Aredes, L. F. D. Silva, G. F. Gontijo, T. C. Tricarico, and J. Posada, "An enhanced shunt active filter based on synchronverter concept," *IEEE J. Emerg. Sel. Topics Power Electron.*, vol. 10, no. 1, pp. 494–505, Feb. 2022.

[22] J. C. Giacomini, L. Michels, H. Pinheiro, and C. Rech, "Active damping scheme for leakage current reduction in transformerless three-phase grid-connected PV inverters," *IEEE Trans. Power Electron.*, vol. 33, no. 5, pp. 3988–3999, May 2018.

[23] D. Sun, X. Wang, H. Nian, and Z. Q. Zhu, "A sliding-mode direct power control strategy for DFIG under both balanced and unbalanced grid conditions using extended active power," *IEEE Trans. Power Electron.*, vol. 33, no. 2, pp. 1313–1322, Feb. 2018.

[24] Y. Zou, L. Zhang, Y. Xing, Z. Zhang, H. Zhao, and H. Ge, "Generalized Clarke transformation and enhanced dual-loop control scheme for three-phase PWM converters under the unbalanced utility grid," *IEEE Trans. Power Electron.*, vol. 37, no. 8, pp. 8935–8947, Aug. 2022.

[25] S. Dai, J. Wang, Z. Sun, and E. Chong, "Model inaccuracy analysis and compensation of stationary frame-based deadbeat predictive current control for high-speed PMSM drives," *IEEE Trans. Transport. Electrific.*, vol. 8, no. 2, pp. 2654–2666, Jun. 2021.

[26] G. C. Leandro, K. Sano, and N. Okada, "A variable admittance shunt capacitor using series inverter for filtering harmonics of distribution systems," *IEEE J. Emerg. Sel. Topics Power Electron.*, vol. 10, no. 3, pp. 3087–3099, Jun. 2021.

[27] J. S. Goud, R. Kalpana, B. Singh, and S. Kumar, "A global maximum power point tracking technique of partially shaded photovoltaic systems for constant voltage applications," *IEEE Trans. Sustain. Energy*, vol. 10, no. 4, pp. 1950–1959, Oct. 2019.

[28] N. Kumar, V. Saxena, B. Singh, and B. K. Panigrahi, "Intuitive control technique for grid connected partially shaded solar PV-based distributed generating system," *IET Renew. Power Gener.*, vol. 14, no. 4, pp. 600–607, Mar. 2020.

[29] A. K. Dubey, J. P. Mishra, and A. Kumar, "Modified CCF based shunt active power filter operation with dead-band elimination for effective harmonic and unbalance compensation in 3-phase 3-wire system," *IEEE Trans. Power Del.*, vol. 37, no. 3, pp. 2131–2142, Jun. 2021.

[30] S. Prakash, J. K. Singh, R. K. Behera, and A. Mondal, "A type-3 modified SOGI-PLL with grid disturbance rejection capability for single-phase grid-tied converters," *IEEE Trans. Ind. Appl.*, vol. 57, no. 4, pp. 4242–4252, Jul. 2021.

[31] P. Kanjiya, V. Khadkikar, and M. S. El Moursi, "Adaptive low-pass filter based DC offset removal technique for three-phase PLLs," *IEEE Trans. Ind. Electron.*, vol. 65, no. 11, pp. 9025–9029, Nov. 2018.

[32] *Photovoltaic (PV) Systems—Characteristics of the Utility Interface*, Standard IEC 61727:2004, 2004.

[33] A. Dash, U. R. Muduli, S. Prakash, K. A. Hosani, S. R. Gongada, and R. K. Behera, "Modified proportionate affine projection algorithm based adaptive DSTATCOM control with increased convergence speed," *IEEE Access*, vol. 10, pp. 43081–43092, 2022.

[34] H. A. Attia, T. K. S. Freddy, H. S. Che, W. P. Hew, and A. H. El Khateb, "Confined band variable switching frequency pulse width modulation (CB-VSF PWM) for a single-phase inverter with an LCL filter," *IEEE Trans. Power Electron.*, vol. 32, no. 11, pp. 8593–8605, Nov. 2017.

[35] J. K. Singh, K. A. Jaafari, R. K. Behera, K. A. Hosani, and U. R. Muduli, "Faster convergence controller with distorted grid conditions for photovoltaic grid following inverter system," *IEEE Access*, vol. 10, pp. 29834–29845, 2022.

[36] A. B. Acharya, D. Sera, L. E. Norum, and R. Teodorescu, "Frequency adaptive digital filter implementation of proportional-resonant controller for inverter applications," in *Proc. IEEE 19th Workshop Control Model. Power Electron. (COMPEL)*, Jun. 2018, pp. 1–7.

[37] R. Chattopadhyay, A. De, and S. Bhattacharya, "Comparison of PR controller and damped PR controller for grid current control of LCL filter based grid-tied inverter under frequency variation and grid distortion," in *Proc. IEEE Energy Convers. Congr. Expo. (ECCE)*, Sep. 2014, pp. 3634–3641.

BIBHUTI BHUSAN RATH received the B.E. degree in electrical engineering from Utkal University, Bhubaneswar, India, in 1998, and the M.Tech. degree in electrical engineering from Jawaharlal Nehru Technological University, Hyderabad, India, in 2011. He is currently pursuing the Ph.D. degree in electrical engineering from the Govind Ballabh Pant Institute of Engineering and Technology, Pauri Garhwal, Uttarakhand, India. His research interests include the design of classical and intelligent controllers for solar photovoltaic power systems and the application of soft computing methods in electric power systems.

MANOJ KUMAR PANDA (Senior Member, IEEE) received the B.E. degree in electrical engineering and control instrumentation from Utkal University, India, in 1998, the M.E. degree in electrical engineering and control instrumentation from the Motilal Nehru National Institute of Technology Allahabad, India, in 2002, and the Ph.D. degree in control system engineering from the Indian Institute of Technology Roorkee, India, in 2014. He is currently working as a Professor with the Department of Electrical Engineering, Govind Ballabh Pant Institute of Engineering and Technology, Pauri Garhwal, Uttarakhand, India. He is an Expert Member of National Board of Accreditation (NBA) wing of MHRD, Govt. of India. His research interests include field of soft computing and its engineering applications, renewable energy, and fuzzy control systems.

BHOLA JHA received the B.Sc. degree in electrical engineering and high voltage engineering from the Muzaffarpur Institute of Technology, Muzaffarpur, Bihar, India, in 1998, the M.Tech. degree in electrical engineering and high voltage engineering from Jawaharlal Nehru Technological University, Hyderabad, India, in 2004, and the Ph.D. degree in electrical engineering from Osmania University, Hyderabad, in 2013. He is currently working as an Associate Professor with the Department of Electrical Engineering, Govind Ballabh Pant Institute of Engineering and Technology, Pauri Garhwal, Uttarakhand, India. His research interests include the design of classical and intelligent controllers for solar photovoltaic power systems and the application of soft computing methods in electric power systems.

AROBINDA DASH (Graduate Student Member, IEEE) received the B.Tech. and M.Tech. degrees in electrical engineering from the Biju Patnaik University of Technology, Odisha, India. He is currently pursuing the Ph.D. degree in electrical engineering with the College of Engineering and Technology, Bhubaneswar, Odisha. He is currently working as a Research Intern in electrical engineering at the Indian Institute of Technology Patna, India. His research interests include renewable energy integration and grid synchronization.

SURYA PRAKASH (Graduate Student Member, IEEE) received the B.Tech. degree in electrical and electronics engineering from the Jawaharlal Nehru Technological University Hyderabad (JNTUH), Hyderabad, India, in 2009, and the M.Tech. degree in power electronics engineering from the Visvesvaraya National Institute of Technology (VNIT), Nagpur, Maharashtra, in 2012. He is currently a Research Scholar with the Department of Electrical Engineering, Indian Institute of Technology (IITP), Patna, Bihar, India. His research interests include control methods for power electronics converters in distribution systems and renewable energy resources, grid interconnection issues, power quality enhancement, and low-voltage ride-through.

RANJAN KUMAR BEHERA (Senior Member, IEEE) received the B.Eng. degree in electrical engineering from the Regional Engineering College (NIT) Rourkela, India, in 1998, and the M.Tech. and Ph.D. degrees from the Indian Institute of Technology Kanpur, India, in 2003 and 2009, respectively. Since 2009, he has been a Faculty Member and he is currently an Associate Professor at the Department of Electrical Engineering, Indian Institute of Technology Patna, India. His research interests include nonlinear control theory application to power electronic converters, pulse width modulation techniques, and multiphase electric drives control. He was a recipient of the 2022 IEEE Outstanding Paper Award for the IEEE TRANSACTIONS ON INDUSTRIAL ELECTRONICS.

KHALIFA AL HOSANI (Senior Member, IEEE) received the B.Sc. and M.Sc. degrees in electrical engineering from the University of Notre Dame, Notre Dame, IN, USA, in 2005 and 2007, respectively, and the Ph.D. degree in electrical and computer engineering from The Ohio State University, Columbus, OH, USA, in 2011. He is currently an Associate Professor with the Department of Electrical and Computer Engineering, Khalifa University, Abu Dhabi, United Arab Emirates. He is the Co-Founder of the Power Electronics and Advanced Sustainable Energy Center Laboratory, ADNOC Research and Innovation Center, Abu Dhabi. His research interests include a wide range of topics including nonlinear control, sliding mode control, control of power electronics, power systems stability and control, renewable energy systems modeling and control, smart grid, microgrid and distributed generation, and application of control theory to oil and gas applications.

SRINIVASARAO TEGALA (Member, IEEE) received the B.E. degree in electrical and electronics engineering from Andhra University, India, in 2000, the M.E. degree in power systems engineering from Jawaharlal Nehru Technological University, Hyderabad, in 2007, and the Ph.D. degree in electrical engineering from Andhra University, in 2017. He is currently working as a Professor and the Head of the Department of Electrical and Electronics Engineering at the Avanthi Institute of Engineering and Technology, Visakhapatnam, India. His research interests include power system analysis, power system stability, renewable energy integration, microgrid, and high voltage engineering.

UTKAL RANJAN MUDULI (Member, IEEE) received the B.Tech. degree in electrical and electronics engineering from the Biju Patnaik University of Technology, Rourkela, Odisha, India, in 2011, the M.Tech. degree in electrical engineering from the Indian Institute of Technology Gandhinagar, India, in 2014, and the Ph.D. degree in electrical engineering from the Indian Institute of Technology Patna, India, in 2022. He was a Visiting Scholar and a Research Associate with the Department of Electrical Engineering and Computer Science, Khalifa University, United Arab Emirates, in 2019 and 2021, respectively, where he is currently working as a Postdoctoral Research Fellow. His research interests include modulation strategies for multiphase motor drives, matrix converters and its control, battery power management, and wireless power transfer. He was a recipient of the 2022 IEEE Outstanding Paper Award for the IEEE TRANSACTIONS ON INDUSTRIAL ELECTRONICS.